Contents lists available at ScienceDirect

Additive Manufacturing

Solidification behavior and porosity in electron-beam powder bed fusion of Co–Cr–Mo alloys: Effect of carbon concentrations

Shoya Aota [a,b,1], Kenta Yamanaka [a,*], Manami Mori [a,c], Nobuyuki Sasaki [a,2], Jérôme Adrien [d], Eric Maire [d], Damien Fabrègue [d,e], Akihiko Chiba [a]

[a] *Institute for Materials Research, Tohoku University, 2-1-1 Katahira, Aoba-ku, Sendai 980-8577, Japan*
[b] *Department of Materials Processing, Graduate School of Engineering, Tohoku University, 6-6-02 Aoba-yama, Aoba-ku, Sendai 980-8579, Japan*
[c] *Department of General Engineering, National Institute of Technology, Sendai College, 48 Nodayama, Medeshima-Shiote, Natori 981-1239, Japan*
[d] *Université de Lyon, INSA-Lyon, MATEIS, UMR CNRS 5510, 20 Avenue Einstein, 69621 Villeurbanne, France*
[e] *ELyT Max, UMI 3757, CNRS, Université de Lyon–Tohoku University, International Joint Unit, Tohoku University, Sendai 980-8577, Japan*

ARTICLE INFO

ABSTRACT

An increased carbon content strengthens Co–Cr–Mo alloys for use in a broad range of industrial applications. In this study, we investigated the influence of the carbon content (0.04–2.5 mass%) on the porosity and microstructure of Co–27Cr–6Mo (mass%) alloys during atomization and electron-beam powder bed fusion (EB-PBF). Quantitative X-ray computed tomography clarified that the volume fraction of pores in the raw powders monotonically increased with the carbon content, as a potential effect of the significant reduction in the liquidus temperature. In contrast, the porosity evolution in the investigated alloys during EB-PBF under identical building conditions suggested an influence of carbon concentration that was distinct from that in the powder. These alloys exhibited negligible porosity fraction for 0.04 and 0.22 mass% and a maximum volume fraction (~0.3 vol.%) at 2.0 mass%, followed by a remarkable reduction caused by further carbon addition. The porosity of the as-built alloys could be correlated to the solidification behavior varying with carbon concentration. The smoother and more flat solidification front during the cellular (0.04 and 0.22 mass%) and eutectic (2.5 mass%) solidification could effectively eliminate the gas bubbles from the melt pool, whereas the complicated morphology at the solid–liquid interfaces during the dendritic growth (1.5 and 2.0 mass%) hindered the pore elimination in the melt pool. Adding carbon significantly increased the Rockwell hardness of the as-built specimens, reaching a significantly high value of HRC59 at 2.5 mass% of carbon, primarily due to the formation of hard carbide precipitates. The obtained findings could be beneficial to reduce entrapped gas pores thereby contributing to the development of highly durable metal components.

1. Introduction

Co–Cr–Mo alloys have been widely used in biomedical applications such as artificial hip/knee joints, spinal instrumentation devices, and dental restorations owing to their excellent combination of wear resistance, corrosion resistance, mechanical properties, and biocompatibility [1–5]. The further development of the mechanical and biological properties of highly durable implants with prolonged service lives is still required despite the abundant clinical achievements. Various studies have been conducted to improve the performance of Co–Cr–Mo alloys

via alloy design and thermomechanical processing [6–14]. A novel process is required for manipulating the microstructure and properties of the designed alloys; this is because the typical processing of alloys via plastic deformation is challenging due to limitations in the capability of these techniques to control microstructure and geometry.

Additive manufacturing (AM) is a promising manufacturing technology that enables the fabrication of complex geometries and the tailoring of the microstructures and mechanical properties of metallic materials [15–20]. The electron-beam powder-bed-fusion (EB-PBF) [21–24] process utilizes an electron beam as a heat source to selectively

melt the thin raw powder layer (powder bed) in a vacuum environment. It offers several advantages such as a sufficiently high energy density for melting refractory metals [25,26], a high scanning speed, and low residual stress, thereby rendering it suitable for fabricating high-quality metal components.

One of the vital materials that have been produced using EB- [27–31] and laser (L)-PBF [32–38] are biomedical Co–Cr–Mo alloys, whose compositions satisfy the ASTM F75 standard. The as-built Co–Cr–Mo alloys prepared using PBF techniques exhibit a columnar microstructure of the face-centered cubic (FCC) γ-phase [22,30–32]. Carbide precipitation is observed in the as-built microstructures of the alloy after EB-PBF. Sun et al. [27] reported that the $M_{23}C_6$-type carbide precipitates formed in the Co–28Cr–6Mo–0.23C–0.17N alloy at the columnar grain boundaries along the build direction (BD). Tan et al. [28] demonstrated using atom probe tomography and transmission electron microscopy that two types of carbides, i.e., $M_{23}C_6$ and M_6C, coexisted in EB-PBF Co–28.50Cr–6.00Mo–0.22C–0.15N alloy components.

The EB-PBF process is capable of producing homogeneously distributed fine carbide precipitates in biomedical-grade Co–Cr–Mo alloys that are unobtainable via casting, rendering it an attractive method for manipulating the microstructure and mechanical properties of the alloy. Moreover, alloys with high carbon contents that cannot be handled in conventional processing routes (e.g., hot forging) are processable using PBF. Therefore, we examined the possibility of processing high-carbon Co–Cr–Mo alloys (up to 2.5 mass%) via EB-PBF for industrial applications, e.g., cutting tools for corrosive environments such as seawater. Fig. 1 shows a vertical section of the phase diagram for the Co–27Cr–6Mo–xC (mass%) system, as calculated using Thermo-Calc software (Thermo-Calc 2022a, Database: TCNI8: Ni-Alloys v8.6). The FCC γ-phase exists as the primary phase solidified from the liquid phase. Increasing the carbon content potentially enhances the hardness of alloys owing to the increased amount of hard carbide phases ($M_{23}C_6$ and M_7C_3). In contrast, the solidification behavior will be altered depending on the carbon content, which in turn affects the microstructural features. Increasing the carbon content significantly reduces the liquidus temperature, and the alloy containing approximately 2.5 mass% of carbon is located near the eutectic composition.

The powder characteristics also affect the quality of the built components [39–41]. Notably, pores in the raw powder remain in the as-built specimens, even in cases where the relative density of the as-built components was extremely close to 100%, and these pores often act as crack initiation sites during fatigue loading [42–46]. Although hot isostatic pressing is employed to fill such pores and enhance the fatigue properties, the entrapped gas pores cannot be completely eliminated in principle [45]. A solution is to reduce the pores in the raw powders and eliminate the powder-originated pores during the subsequent EB-PBF process.

X-ray computed tomography (XCT) is an exhaustive method to detect pores and quantify their size and shape inside the bulk of a material [47, 48]. Laboratory-based XCT is sufficient to detect large (>10 μm in size) pores in X-ray absorbent samples [49].

In this study, to fundamentally understand the correlation between the solidification behavior and porosity, we examined the effect of carbon concentration on the porosity of the raw powder and its variation in the bulk specimens during EB-PBF using XCT. The results revealed that an alteration in the solidification mechanism with the carbon content significantly affected the porosity of both the raw powder and as-built components in addition to the microstructural and mechanical characteristics.

2. Material and methods

2.1. Raw powders

In this study, we prepared five different Co–27Cr–6Mo–xC (mass%) alloy powders with varying carbon contents (0.04–2.5 mass%). The chemical compositions of the prepared powders are listed in Table 1. The concentrations of the constituent metallic elements were determined using inductively coupled plasma optical emission spectrometry (ICP-OES) (ARCOS FHM22 MV130, SPECTRO Analytical Instruments, Germany), while the nitrogen concentrations were determined using the He carrier fusion-thermal conductivity method (ON836, LECO, USA). The carbon concentrations were determined using the combustion-infrared absorption method (CS844, LECO, USA). Hereafter, according to their carbon content, these alloys are referred to as the 0.04C, 0.22C, 1.5C, 2.0C, and 2.5C alloys, among which the 0.04C and 0.22C alloy powders satisfy the ASTM F75 standard for biomedical applications. The 0.22C powder was produced at AP&C (Canada) but procured from Arcam (Sweden). The other powders were produced by Ar-gas atomization after the vacuum induction melting of raw materials at Sanyo Special Steel (Japan).

Thin-wall specimens with a cross-section of 20 mm × 2 mm and a height of 20 mm were manufactured by the Arcam A2X system using five distinct carbon-content powders. The sample dimensions were determined by considering industrial cutters as a potential application. Support structures with a height of 5 mm were used beneath the specimens. Identical building conditions (as stated in Table 2) were employed for each powder to isolate and examine the influence of the carbon content. The building parameters were determined based on the standard conditions for the Arcam Co–Cr–Mo alloy powder. The powder bed was preheated at 850 °C to suppress the "smoke" caused by the accumulation of negative charges in the raw powder [50,51]. The Rockwell hardness (HRC) of the as-built specimens was determined using DXT-10 equipment (Matsuzawa, Japan).

2.2. Particle size distribution measurement

The particle size distributions of the prepared powders were analyzed using a laser-diffraction particle size distribution measuring apparatus (LS230, Beckman Coulter, USA). The particle diameters of 10%, 50%, and 90% of the cumulative particle size distributions are denoted with d_{10}, d_{50}, and d_{90}, respectively. ΔH denotes a value representing the particle size range in the particle size distribution, which was calculated using the following equation:

$$\Delta H = d_{90} - d_{10}. \tag{1}$$

2.3. Surface and cross-sectional characterization

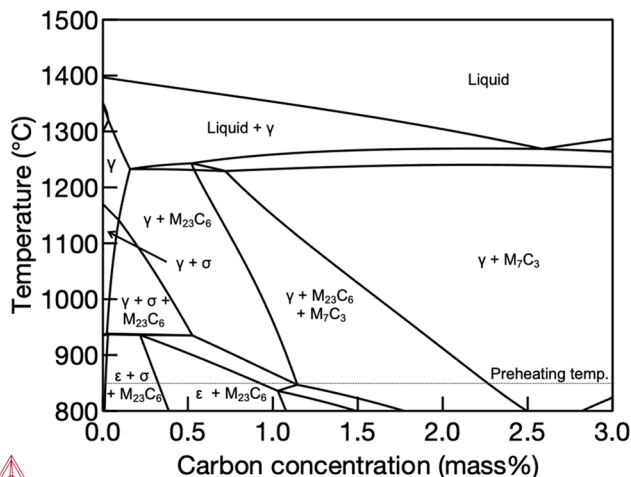The surfaces of the powders and as-built specimens were recorded

Fig. 1. Vertical section of the phase diagram for the Co–27Cr–6Mo–xC (mass%) system calculated using Thermo-Calc software.

Table 1

Chemical compositions of raw powders prepared in this study (mass%).

Alloy	Co	Cr	Mo	Ni	Si	Mn	Fe	N	C
0.04C	Bal.	27.0	5.86	< 0.05	0.40	0.53	0.09	0.11	0.03
0.22C	Bal.	27.1	5.60	< 0.05	0.25	0.55	0.32	0.13	0.21
1.5C	Bal.	26.6	5.85	< 0.05	0.41	0.55	0.12	0.04	1.40
2.0C	Bal.	26.1	5.87	< 0.05	0.38	0.53	0.10	0.03	1.91
2.5C	Bal.	26.3	5.95	< 0.05	0.41	0.54	0.15	0.02	2.47

Table 2

Building parameters employed in this study.

Parameter	Value
Preheating temperature (℃)	850
Beam current (mA)	5.5
Speed function (–)	25
Focus offset (mA)	15
Line offset (mm)	0.2
Layer thickness (µm)	70

Fig. 2. Particle size distributions of raw powders used in this study.

using scanning electron microscopy (SEM, S-3400, Hitachi High-Technologies, Japan) operated at 15 kV. The corresponding cross-sectional images were acquired using field-emission SEM (FE-SEM, JSM-7100 F, JEOL, Japan) at an accelerating voltage of 15 kV. Electron backscatter diffraction (EBSD) scans of the as-built specimens were performed using a field-emission SEM (FE-SEM) (XL30S-FEG, FEI, USA) operated at 20 kV. The EBSD data were acquired and analyzed using a TSL-OIM system (ver. 7.3, EDAX, USA). The precipitates formed in the as-built samples were investigated using field-emission electron probe microanalysis (FE-EPMA, JXA-8530 F, JEOL, Japan) at an acceleration voltage of 15 kV. These microstructural characterizations were performed at the middle height of each as-built specimen. The samples for SEM, EBSD, and EPMA were prepared by mechanical grinding using emery paper (up to #3000, Struers, Japan), polishing with a 0.3 µm alumina suspension (AP-A, Struers, Japan), and finally mirror-finishing using a 0.04 µm colloidal silica solution (OP-U, Struers, Japan).

2.4. XCT analysis

The morphology, size, and fraction of pores inside the raw powders and as-built samples were quantitatively investigated by performing XCT static scans using a Phoenix V|tome|x system (GE, USA) [52] with an accelerating voltage of 100 kV. The raw powders were encapsulated into a polymer tube with an inner diameter of 3 mm for XCT measurements. The as-built samples were machined into the dimensions illustrated in Fig. S1, and they were designed for the in-situ XCT experiments involving tensile loading. The whole gauge portion of each specimen was analyzed with a voxel size of 2.0 µm and 1.5 µm for the powders and as-built specimens, respectively. Each sample was spanned over 360°, and 1200 projection images were captured at an increment of 0.3° during scanning with an exposure time of 333 ms for each projection and a total acquisition time of 25 min. The pores in the powders and as-built specimens were detected and separated from the slice images using 3D ImageJ Suite [53]. The separation routine is described in Ref. [54]. The three-dimensional structures of the separated pores in the powders and as-built samples were reconstructed, and a quantitative porosity analysis was performed using Fiji ImageJ [55].

3. Results

3.1. Powder size and morphology

The particle size distribution of the prepared powders is illustrated in Fig. 2, wherein the results for the commercial 0.22C powder displayed a single peak at approximately 50 µm. The other powders, i.e., 0.04C, 1.5C, 2.0C, and 2.5C, exhibited bimodal distributions as a product of not
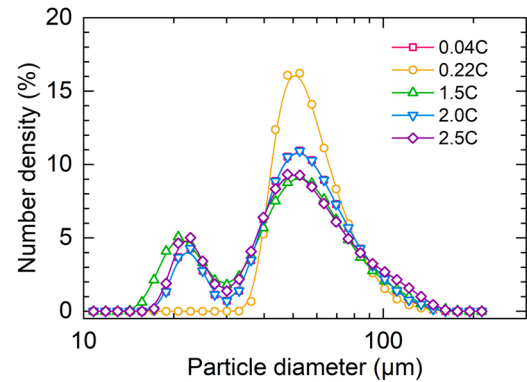
being sieved. In addition, a major peak existed at approximately 50 µm, which was similar to that of the 0.22C powder. A minor peak was present at approximately 20 µm for the gas-atomized powders. The fraction of the larger particles with a particle size range of 100–140 µm was higher in the 2.0C and 2.5C powders, suggesting an increase in size with the carbon content.

The d_{10}, d_{50}, and d_{90} values of the prepared powders are summarized in Table 3. The d_{50} values did not exhibit a significant difference between the alloys, located at approximately 50 µm for all the powders. The ΔH value of the 2.5C powder was the largest (65 µm), whereas that of the 0.22C powder was the smallest (35 µm), as this powder did not contain finer particles at ~20 µm (Fig. 2).

The surface morphologies of the powders are depicted in Fig. 3, which demonstrates that all powders were predominantly spherical. Secondary particles (i.e., satellites) were attached to the surfaces of the larger particles in all the prepared powders, thereby producing aggregates as non-spherical particles. Thus, the minor peaks at approximately 20 µm in Fig. 2 for the gas-atomized powders were attributed to the satellite particles generated during gas atomization.

3.2. Powder microstructures

Cross-sectional SEM-backscattered electron (BSE) images of the prepared powders are portrayed in Fig. 4. The 0.04C and 0.22C powders represented similar microstructures comprising relatively equiaxed grains at the given cross-sections. Some bright regions were observed at the grain boundaries, denoting secondary-phase precipitation. Fine dendritic microstructures were observed for the alloy powders with carbon contents ≥ 1.5 mass%, and nanosized precipitates were observed in the interdendritic regions of the 2.5C alloy powder (Fig. 4(e)).

Table 3

Particle sizes of raw powders prepared in this study.

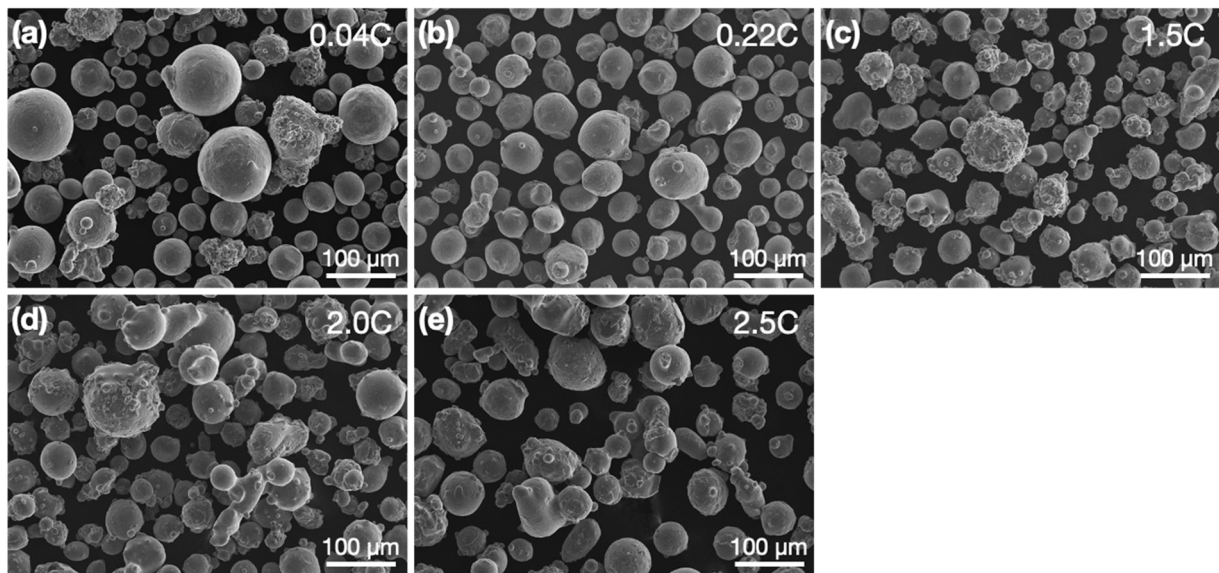| Alloy	d_{10} (µm)	d_{50} (µm)	d_{90} (µm)	ΔH (µm)
0.04C	23	50	80	57
0.22C	41	52	76	35
1.5C	20	47	79	59
2.0C	23	50	81	57
2.5C	22	49	87	65

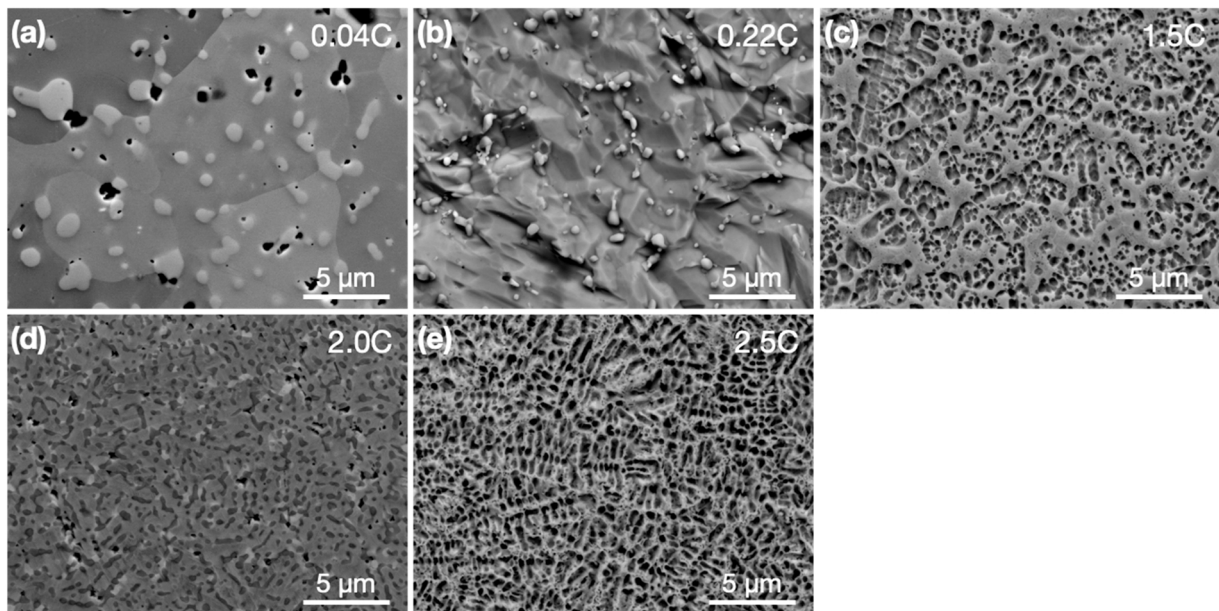**Fig. 3.** SEM images of (a) 0.04C, (b) 0.22C, (c) 1.5C, (d) 2.0C, and (e) 2.5C powders.

Fig. 4. Cross-sectional SEM-BSE images of (a) 0.04C, (b) 0.22C, (c) 1.5C, (d) 2.0C, and (e) 2.5C powders.

3.3. Volume fraction and size distribution of pores in the powders

The cross-sectional XCT images of the prepared powders are presented in Fig. 5, wherein pore sizes ranging from several micrometers to several tens of micrometers were detected in some granules of the five alloy powders, regardless of the carbon content. The closed pores were separated from these data to reconstruct the three-dimensional (3D) images of these internal pores, as depicted in Fig. 6 (see also Video S1 in the Supplementary Material). The reconstructed 3D images revealed that the pores were spherical and uniformly distributed throughout the powder.

Supplementary material related to this article can be found online at doi:10.1016/j.addma.2022.103134.

The volume fraction of the pores in the raw powders is presented in Fig. 7, as calculated from the 3D reconstructed XCT results by dividing the pore volume by the powder volume. It was unveiled that the 0.04C powder exhibited the lowest porosity (~0.09 vol.%), and the porosity of

the 0.22C powder was almost equivalent to that of the 0.04C powder. A further increase in the carbon content ($\geq$1.5 mass%) significantly increased the volume fraction of pores in the gas-atomized powders, with the 2.5C powder displaying the highest pore content of approximately 0.37 vol.%.

The size distributions of pores for each composition are shown in Fig. 8(a−e). The pores observed were dominantly lower than 25 μm in diameter. Larger pores in the diameter range of 25–45 μm can be seen exclusively in the histograms of the high-carbon ($\geq$1.5 mass%) powders. The relationship between the maximum pore diameter and carbon content is depicted in Fig. 8(f). The porosity was similar for the 0.04C and 0.22C powders and was significantly increased in the high-carbon powders, following an approximately linear trend.

The volume fraction of the pores for a specific particle size of each powder is illustrated in Fig. 9, which indicated that the powder porosity increased with the particle size. The porosity of the powders for identical particle sizes increased with the carbon content.
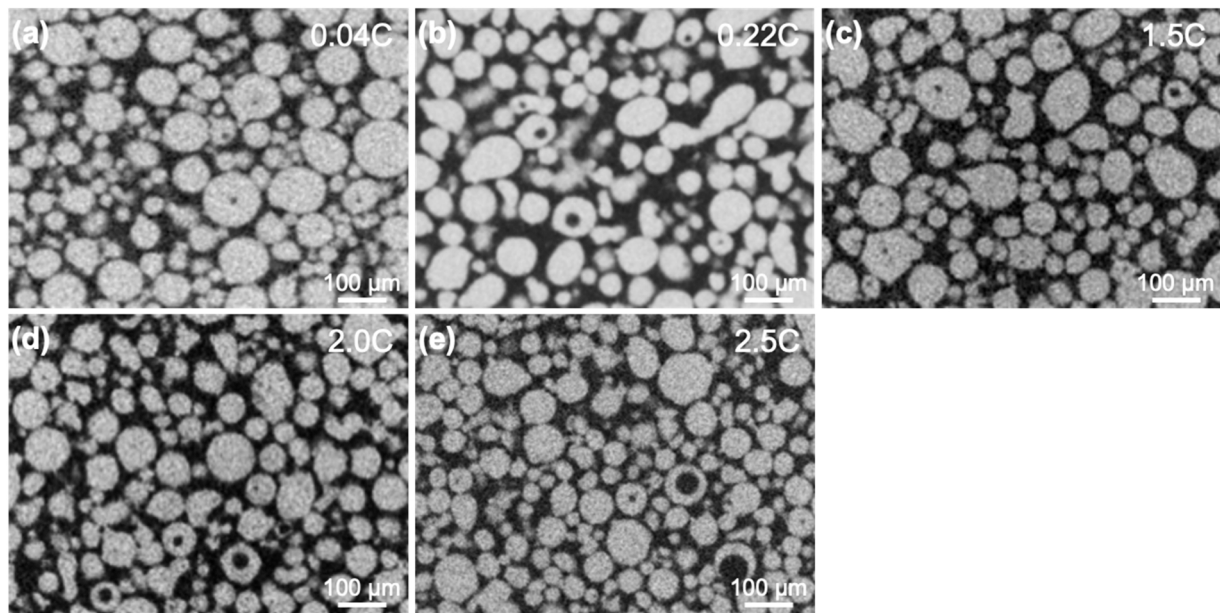
Fig. 5. Cross-sectional morphologies of (a) 0.04C, (b) 0.22C, (c) 1.5C, (d) 2.0C, and (e) 2.5C powders, as obtained by XCT.
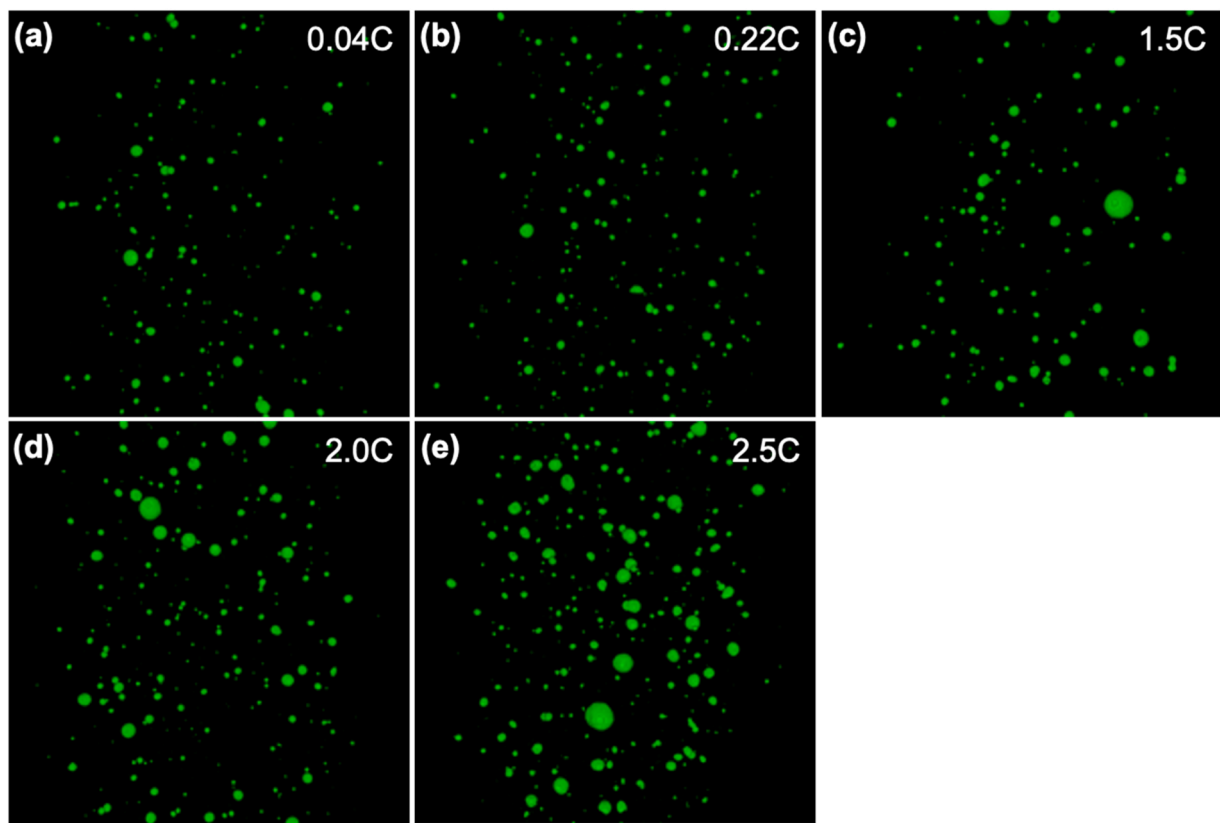

Fig. 6. 3D reconstructed pore morphologies of (a) 0.04C, (b) 0.22C, (c) 1.5C, (d) 2.0C, and (e) 2.5C powders, as obtained by XCT.

3.4. Microstructures of as-built specimens

The SEM-BSE images of the as-built specimens prepared using the EB-PBF under identical building conditions are portrayed in Fig. 10, displaying columnar microstructures growth along the BD in the 0.04C and 0.22C alloys (Fig. 10(a) and 10(b)) with fine precipitates identified along the columnar grain boundaries. The as-built specimens of the 1.5C and 2.0C alloys exhibited well-defined, complicated dendritic

microstructures, as shown in Fig. 10(c) and 10(d), respectively. There are two types of precipitates present, displaying as black and white phases. Notably, well-defined dendrite arms appeared in the 2.5C alloy (Fig. 10(d)). The SEM-BSE images demonstrated that the black phase was formed between the primary dendrite arms, whereas the white phase forming the final solidified portion was observed between the secondary dendrite arms. A further rise in the carbon content to 2.5 mass % produced the gray region containing fine particles, as observed from
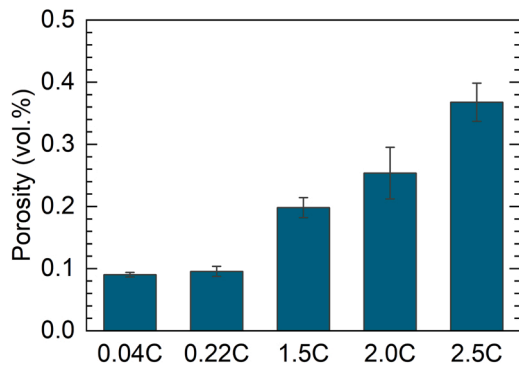
Fig. 7. Volume fraction of porosity in investigated powders as a function of carbon content. The error bars were obtained from multiple XCT measurements.

the SEM-BSE image displayed in Fig. 10(e).

The high-magnification SEM-BSE images and the corresponding EPMA elemental mapping of the as-built specimens are presented in Fig. 11. The 0.04C alloy (Fig. 11(a)) contains precipitates enriched with Cr, Si, and Mo at the columnar grain boundaries, whereas Co was primarily distributed in the grain interior. A similar elemental distribution was observed in the 0.22C alloy specimen, as depicted in Fig. 11(b). These grain boundary precipitates were enriched with carbon, indicating the formation of carbides as a film along the columnar grain boundaries, as reported previously [28]. The elemental mapping of the 1.5C and 2.0C alloys (Fig. 11(c) and 11(d)) revealed that the black and white precipitates in the SEM-BSE images were enriched with Cr and Mo, respectively. In addition, Si was preferentially partitioned into the white phase, and more carbon enrichment was observed in the black precipitates, as represented by a notable concentration difference between the two precipitated phases. Although the morphology of the precipitates significantly varied in the 2.5C alloy, the elemental
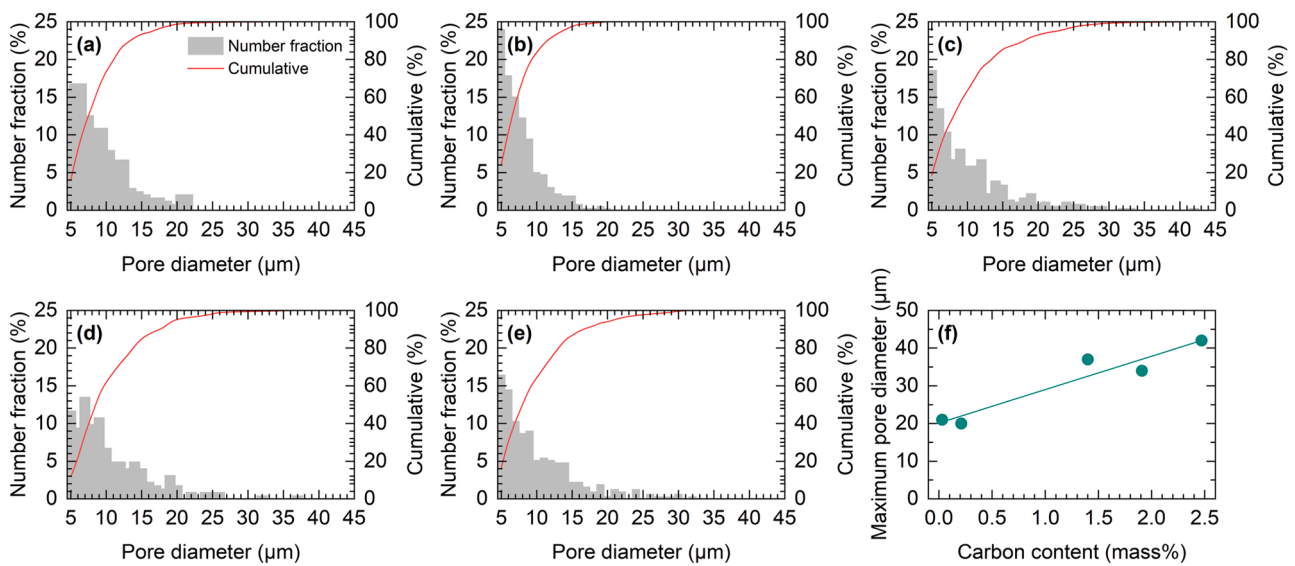

Fig. 8. Pore diameter distributions of pores of (a) 0.04C, (b) 0.22C, (c) 1.5C, (d) 2.0C, and (e) 2.5C powders, as obtained by XCT. (f) Maximum pore diameter in the raw powders as a function of carbon content.
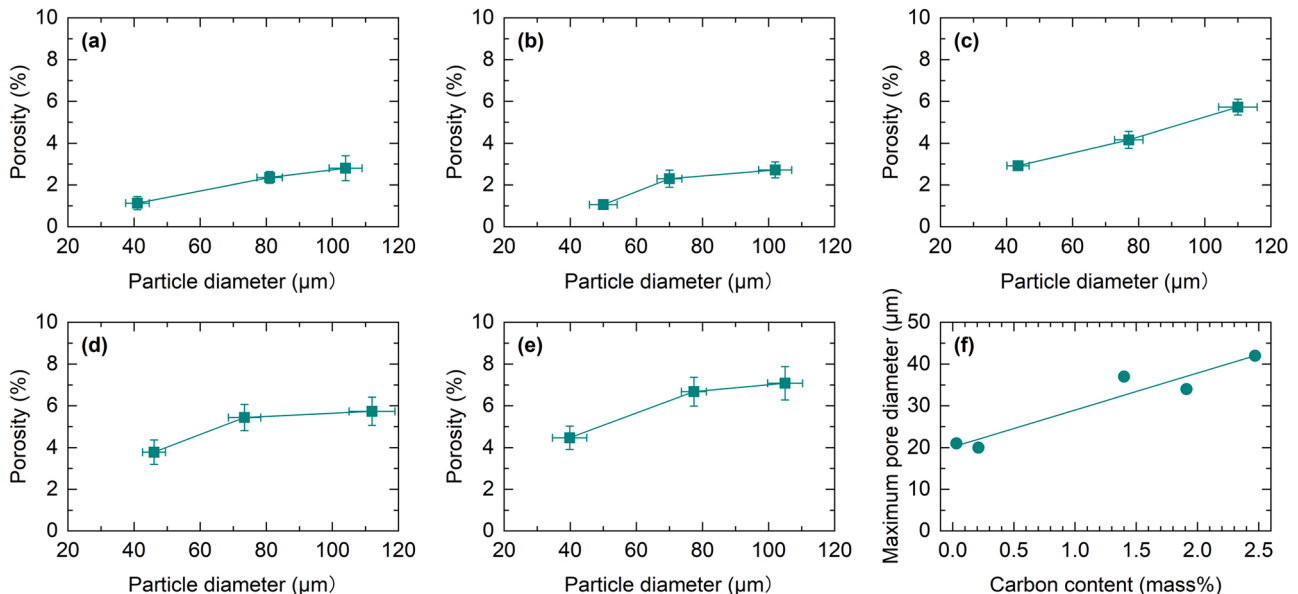

Fig. 9. Volume fraction of porosity in powders at particle sizes: (a) 0.04C, (b) 0.22C, (c) 1.5C, (d) 2.0C, and (e) 2.5C alloys.
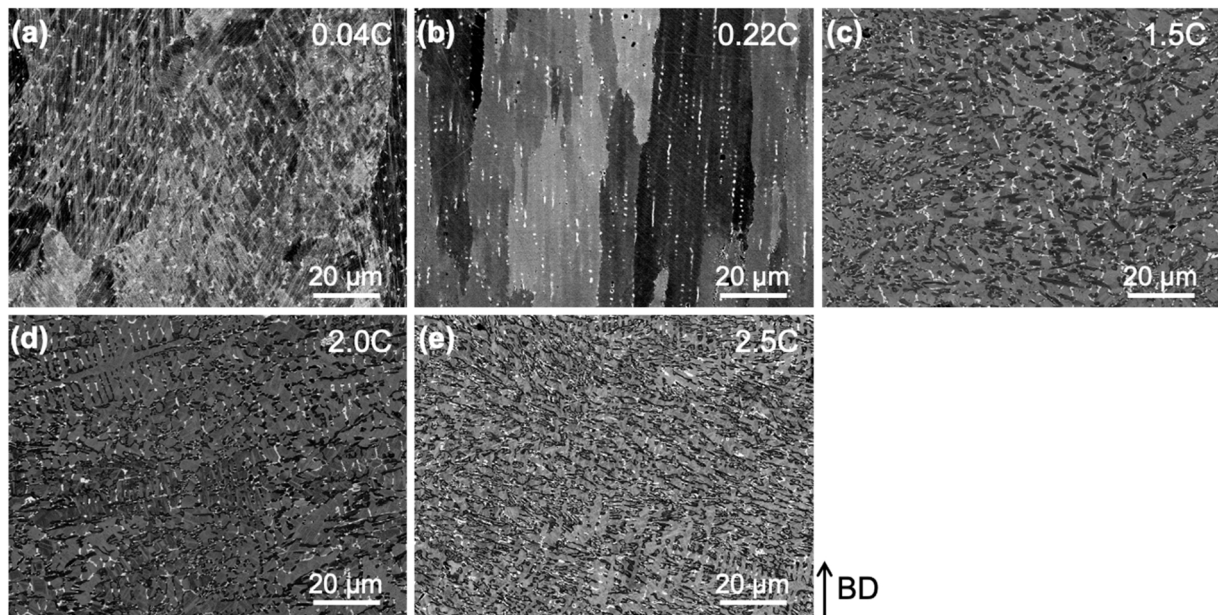
Fig. 10. SEM-BSE images for the as-built specimens produced by the EB-PBF process observed at cross-sections parallel to the BD: (a) 0.04C, (b) 0.22C, (c) 1.5C, (e) 2.0C, and (d) 2.5C alloys.

partitioning tendency remained unchanged (Fig. 11(e)). Nonetheless, the carbon concentration of the carbide phase in the 2.5C alloy seems to be lower than that in the 2.0C alloy, which could be attributed to the distributions of the other alloying elements, such as Mo and Si.

The image quality (IQ), inverse pole figure (IPF), and phase maps of the as-built specimens prepared with EB-PBF are illustrated in Fig. 12, as obtained by the EBSD measurements. The $M_{23}C_6$ carbide is a potential carbide phase in the system [28] that was excluded from the EBSD measurements because the γ-phase and $M_{23}C_6$ carbide could not be easily distinguished as they have similar FCC structures. Only the γ-phase was observed in the 0.04C and 0.22C alloys forming a columnar microstructure that extended along the BD. This showed that the preferred growth orientation of the columnar grains was in the $\langle 001 \rangle_\gamma$ direction aligned with the BD, as observed in biomedical Co–Cr–Mo alloys fabricated using EB-PBF [28,30,31]. The high-carbon alloys (i.e., 1.5C, 2.0C, and 2.5C) did not display such a preferential crystal growth and exhibited more complicated microstructures. The matrices of the 1.5C and 2.0C alloy specimens comprised a combination of the γ-phase and the plate-like ε-phase with a hexagonal close-packed (HCP) structure. The carbide phase appearing with a black contrast in the IQ maps can be indexed as M_7C_3 carbide. The structure of the 2.5C alloy specimen was a duplex γ + ε matrix containing M_7C_3 carbides.

3.5. Porosity in as-built specimens

The cross-sectional XCT images at different depths of each as-built specimen are presented in Fig. 13. The 0.04C alloy specimen displayed negligible pores in the XCT measurements, and a few pores were observed in the 0.22C alloy specimen. The observed pores were primarily spherical, implying that they were generated in the powder particles during the atomization process and remained in the subsequent EB-PBF process. Spherical gas pores were more frequently observed in the as-built specimens with higher carbon contents (1.5–2.5 mass%). The XCT images showed that non-spherical, irregular-shaped defects generated during the EB-PBF process (e.g., lack of fusion) were very rarely observed in the as-built specimens. This suggests the building parameters employed in this study were optimal for the investigation of the varying carbon contents in the alloys.

The influence of carbon concentration on the volume fraction of pores in the as-built specimens, as determined from the XCT

measurements, is presented in Fig. 14, wherein the porosity of the raw powders is depicted for comparison. The porosity was less than 0.2 vol. % irrespective of the carbon content, indicating that all the as-built specimens were almost completely dense. The porosity of the raw powder for each composition decreased during the EB-PBF process. The porosities of 0.04C and 0.22C alloy specimens reduced from ~0.10 vol. % in the raw powder to almost zero for the as-built. The as-built specimens generally displayed lower porosity than that for each raw powder. The porosity of the as-built specimens increased with increasing carbon content and exhibited a maximum value (~0.15 vol.%) for the 2.0C alloy. The porosity of the as-built 2.5C alloy specimen was lower than that of the 2.0C alloy specimen in the as-built state, despite the continuous increase in the pore volume fraction in the raw powder with the carbon content. The 2.5C alloy exhibited the largest difference between the porosities of the raw powder and as-built specimens, thereby demonstrating the remarkable reduction in porosity occurring during the EB-PBF process.

3.6. Rockwell hardness of the as-built specimens

Fig. 15 shows the correlation between the carbon concentration and Rockwell hardness. In thee investigated concentration range, the hardness values increased monotonically with the increasing carbon content. The as-built 2.5C alloy specimen reached HRC59, indicating that adding carbon significantly increased the Rockwell hardness. No clear correlation between the hardness and porosity was noticed; this is reasonable because the fraction, which varied depending on the carbon content, of pores in the as-built specimens was overall lower than 0.3 vol.%. Thus, this improved hardness by adding carbon was shown to be primarily due to the formation of hard carbide precipitates rather than the variation in porosity. In the future, the EB-PBF process will be further optimized, and the microstructure–harness correlation will be examined in more detail.

4. Discussion

4.1. Effect of carbon content on powder characteristics

The pores produced during the gas atomization of the raw powder can be generally classified into gas pores formed by the entrapment of atomization/atmospheric gas in droplets and shrinkage caused by the
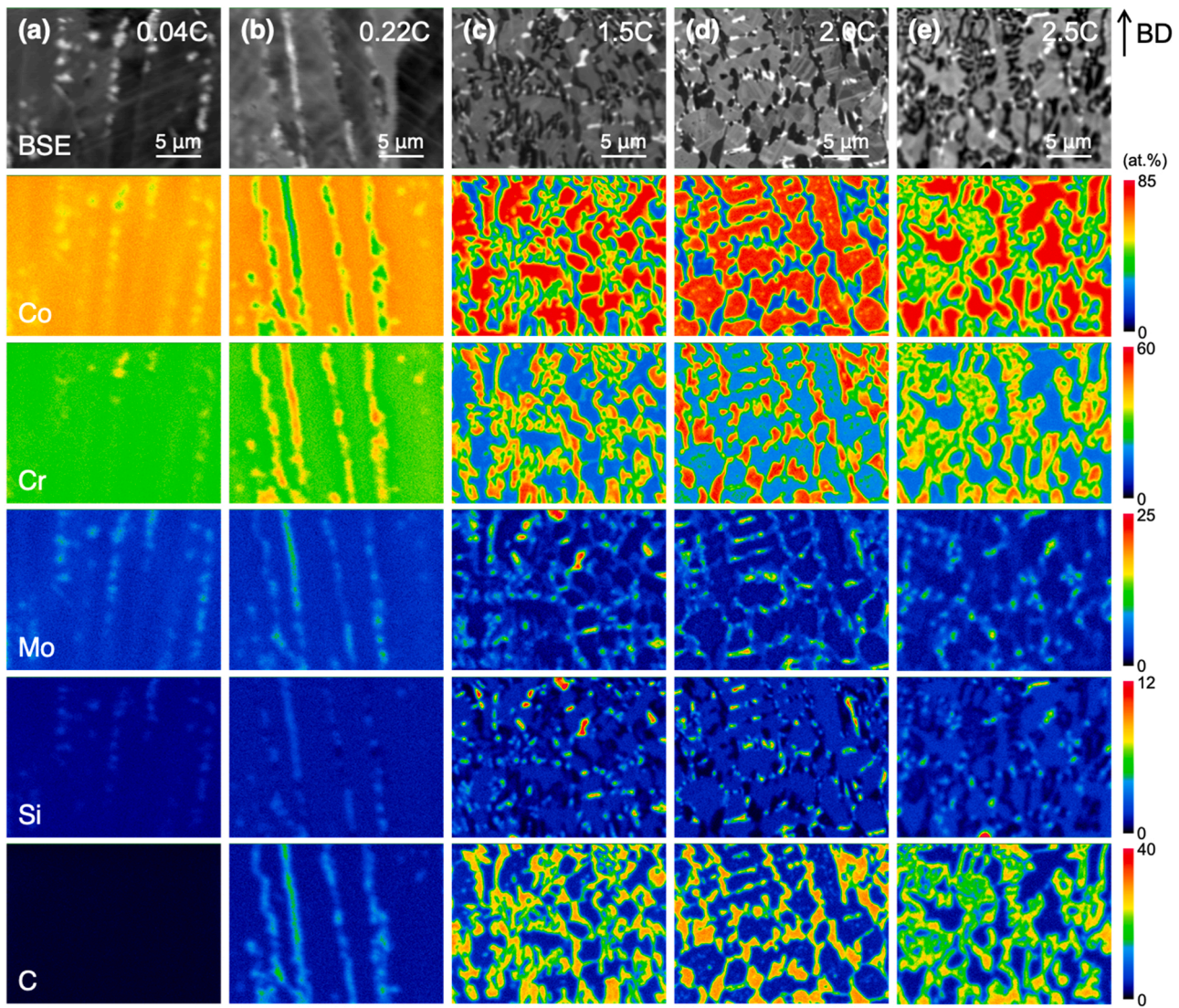
Fig. 11. Cross-sectional EPMA elemental mapping results for the as-built alloy specimens produced by the EB-PBF process: (a) 0.04C, (b) 0.22C, (c) 1.5C, (e) 2.0C, and (d) 2.5C alloys.

volumetric difference between the liquid and solid phases during cooling [56,57]. The reconstructed XCT images displayed in Fig. 5 and 6 reveal that the raw powders predominantly contained spherical pores with smooth surfaces. These pores were generated by trapping the Ar gas in droplets during gas atomization, as reported in the literature [42,58,59]. Rabin et al. [60] proposed a "bag liquid breakup mode" model for the entrapped gas pores where during gas atomization, the molten metal stream is disintegrated using gas jets to form droplets, and spherical particles are obtained because of the surface tension of the molten metal. In this procedure, when a bag liquid break-up mode occurs for the molten metal ejecting from the nozzle depending on the condition: the droplets are deformed into a hollow gas bag and disintegrate into fine particles or the hollow gas bag may close to form a hollow sphere containing a gas pore inside. The behavior depends on the Weber number (*We*) that indicates the ratio between the fluid inertia and surface tension, and can be formulated as follows:

$$We = \frac{\rho d v}{\sigma}, \qquad (2)$$

where ρ, d, v, and σ denote the density of the liquid, initial particle diameter, velocity, and surface tension, respectively. Figs. 8–10 demonstrate that a higher carbon content yields a higher volume

fraction and a larger pore diameter. According to the calculated phase diagram (Fig. 1), the liquidus temperature monotonically decreases by ~130 K as the carbon content increased from 0 to 2.5 mass%. A similar trend is observed for secondary dendrite arm spacing (SDAS) between the 1.5–2.5 C alloys (Fig. S2), indicating the negligible difference in cooling rate during the gas atomization. This shows that the liquid phase of the high-carbon alloys can exist at much lower temperatures leading to droplets experiencing a liquid state for longer during the process. The surface tension of the liquid rapidly increases during cooling, which significantly inhibits the decomposition of the droplets into fine particles and leads to the droplets solidifying in a spherical shape containing gas inside.

The positive correlation between the particle size and porosity in Fig. 9 constitutes a ubiquitous behavior that is observed in various alloys [60]. Eq. (2) suggests that larger droplets result in higher *We* values, implying that droplets can easily deform, and consequently, entrap gases [61]. The lower liquidus temperature and the longer liquid state for the higher carbon content are likely to increase the probability of collision between the droplets in flight and with the wall of the atomization chamber, which forms irregularly shaped coarse particles. The coarse particles exhibited less sphericity (Fig. 3), as shown by the higher fraction of coarser particles in Fig. 2 (100–140 μm). Similar phenomena
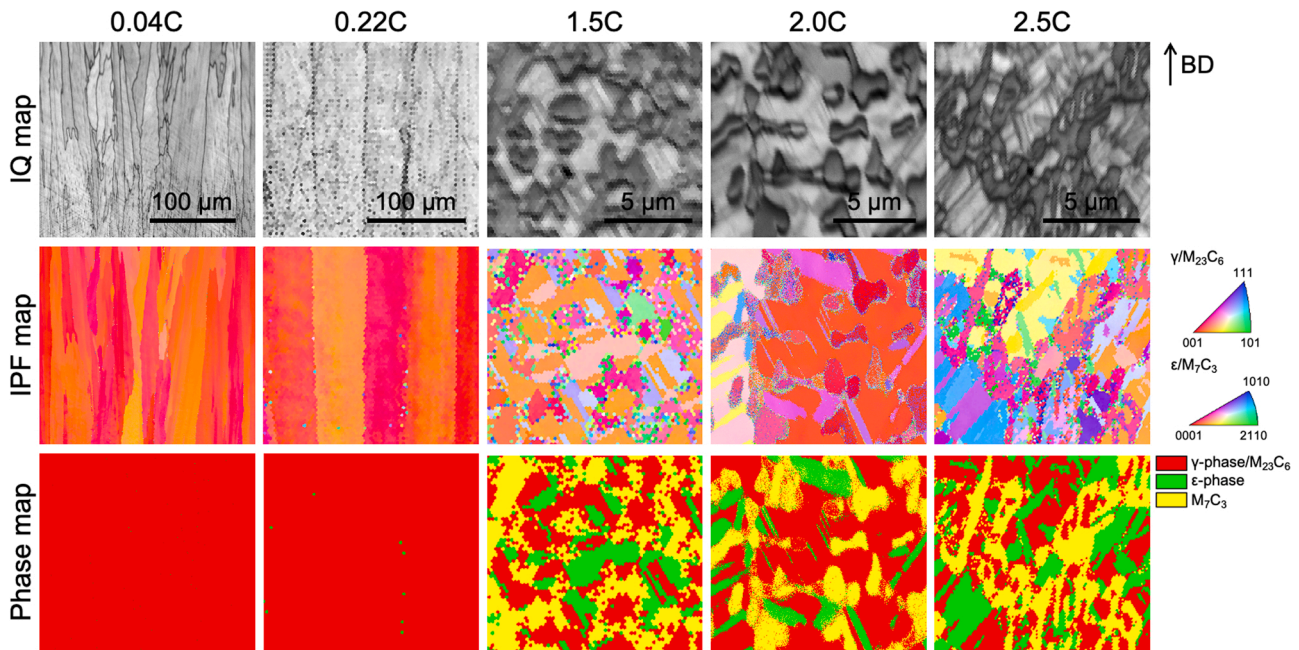
Fig. 12. EBSD results for the as-built specimens. In the IPF maps, the crystallographic orientations along the BD are presented.

have been reported in previous studies on gas-atomized [62] and PREP powders [63].

4.2. Effect of carbon content on microstructural evolution during EB-PBF

The bulk 0.04C alloy specimen fabricated using EB-PBF exhibited a cellular microstructure with precipitates present along the columnar grain boundaries (Figs. 10 and 11). The derived phase diagram shown in Fig. 1 suggests that carbides were not stable for the 0.04C composition. Moreover, EPMA in the as-built 0.04C alloy sample did not show evidence of carbon enrichment in the precipitates (Fig. 11(a)). In contrast, the enrichment of Cr and Mo in the precipitates agrees well with the formation of the σ-phase; the precipitation behavior and partitioning tendency correspond to those in biomedical Co–Cr–Mo alloys with low carbon contents [28]. The σ-phase exists as an equilibrium phase in the low-carbon region of the calculated phase diagram (Fig. 1). Similar precipitates were also observed in the raw powder. The as-built 0.22C alloy sample also exhibited a cellular microstructure and exhibited precipitates at the columnar grain boundaries. Several studies on the EB-PBF of biomedical Co–28Cr–6Mo alloys conforming to the ASTM F75 standard and containing ~0.2 mass% of C [27,28] reported that the precipitated phase was predominantly $M_{23}C_6$ carbide, and those with less Si could correspond to M_6C carbide [28].

The 1.5C and 2.0C alloys exhibited dendritic solidification microstructures with more complicated distributions of the matrix grain and two types of precipitates (Figs. 10–12). The thermodynamic calculations indicated that M_7C_3 carbide existed as a stable carbide phase for Co–27Cr–6Mo–(1.5–2.5)C alloys. The EBSD analysis (Fig. 12) revealed large amounts of M_7C_3 carbide, confirming the black precipitates observed in the SEM-BSE image were M_7C_3 carbides. This large proportion of M_7C_3 carbides is consistent with the thermodynamic calculation results (Fig. 1). The white counterparts in the SEM-BSE image could be the σ-phase, despite not being an equilibrium phase. The 2.5C alloy exhibited a complicated microstructure similar to those observed in the 1.5C and 2.0C alloys. The precipitated phase was M_7C_3 carbide, as detected by the EBSD analysis. The more complex morphology of the precipitated M_7C_3 carbide than that of the other alloys suggests a eutectic reaction. This is reasonable because the 2.5C alloy resembled the eutectic composition (Fig. 1). Accordingly, the 2.5C alloy specimen exhibited a more diffused elemental distribution than the 2.0C alloy

(Fig. 11). The variation in the solidification microstructure with the carbon concentration can be observed in the corresponding powders as well (Fig. 4).

A plate-like ε-phase with an HCP structure was observed in the high-carbon alloy (i.e., 1.5C, 2.0C, and 2.5C) specimens, indicating a γ → ε martensitic transformation during the EB-PBF process [64,65]. The enhanced stability of the γ-phase in the 0.04C and 0.22C alloy specimens could be explained in terms of the nitrogen addition [66,67], whereas the other high-carbon alloys contained less nitrogen (Table 1). Carbon acts as a γ-phase stabilizing element, but a large proportion of carbon in the high-carbon alloys is concentrated in the liquid phase (Fig. 1), which eventually forms carbides during solidification [68,69]. Thus, the formation of the ε-phase indicates a non-equilibrium microstructural evolution. The γ → ε phase transformation negligibly affected the porosity of the as-built alloys because it occurred following a solid-phase transformation.

4.3. Evolution of pores during EB-PBF

The XCT analysis (Fig. 13) detected spherical pores in the as-built samples, implying that the entrapped gas pores in the raw powders remained during the EB-PBF process. The statistical data expressed in Fig. 14 indicate that the EB-PBF specimens displayed a carbon concentration dependence of porosity, which varied from that of the raw powder. The entrapped gas pores for the 0.04C and 0.22C alloy powders were analyzed to be approximately 0.1 vol.%, which were almost completely eliminated to the negligible level during the EB-PBF fabrication. The powders and as-built specimens of the 1.5C and 2.0C alloys exhibited similar levels of porosity for each composition, which exemplified the positive influence of the carbon content on the porosity. The porosity of the 2.5C alloy was significantly reduced during the EB-PBF process such that the maximum porosity was detected in the 2.0C alloy.

The porosity of the EB-PBF specimens relied on the escape of the pre-existing atomization-originated gas pores from the melt pool by migrating to the solid/liquid interfaces during the EB-PBF process. Thus, to reduce pores in the as-built components, the gas bubbles in the melt pool must travel along the melt flow and leave into the surrounding vacuum environment before solidification. Zhan et al. [70] investigated the microstructure and porosity characteristics of an aluminum alloy during laser metal–inert gas hybrid welding and reported that more
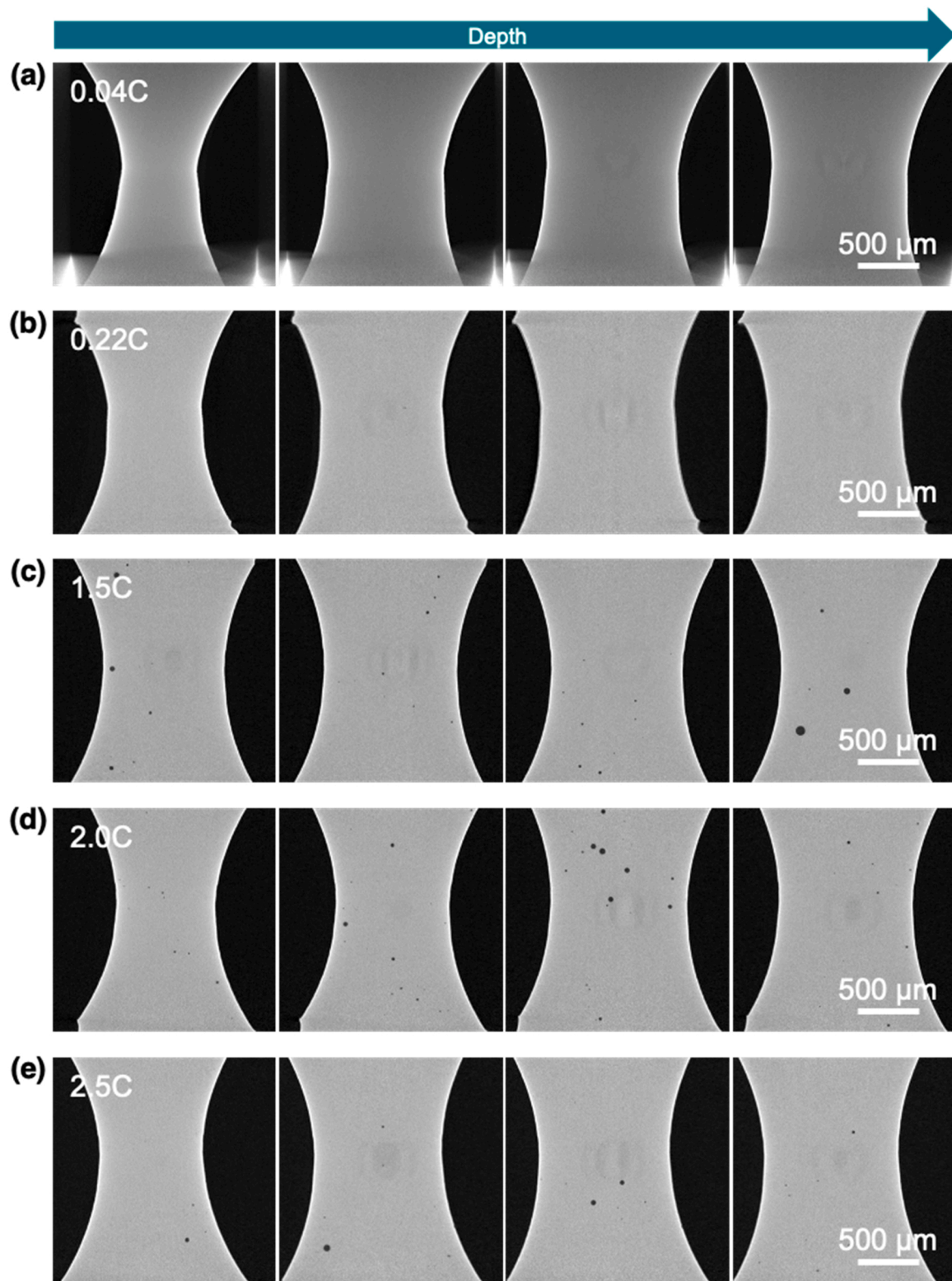
Fig. 13. Cross-sectional morphologies of the as-built alloy specimens at different 2D slice depths, as obtained by the XCT measurements: (a) 0.04C, (b) 0.22C, (c) 1.5C, (e) 2.0C, and (d) 2.5C alloys.

bubbles can be allowed to escape from the melt into the atmosphere if the heat input is increased and a high-temperature melt pool is maintained over a wide area. Hojjatzadeh et al. [71] demonstrated that the high thermocapillary force induced by the high-temperature gradient can rapidly eliminate the pores from the melt pool during the L-PBF process by combining in-situ high-speed high-resolution synchrotron X-ray imaging experiments and multiphysics modeling. Watanabe et al. [72] reported that the temperature dependences of the density, surface tension, and viscosity of Co–27Cr–6Mo alloys hardly vary with the carbon content (0.05 and 0.25 mass%). Although the thermophysical properties of the high-carbon Co–Cr–Mo alloys have not been clarified, Feng et al. [73] conducted a molecular dynamics simulation and found
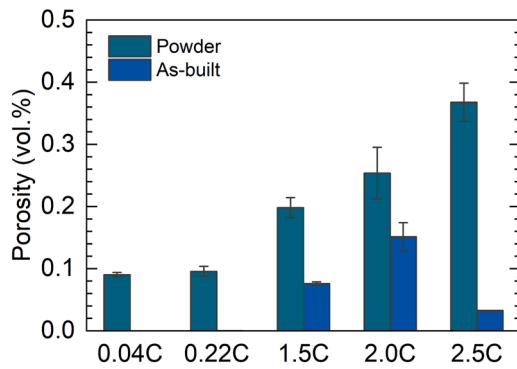
Fig. 14. Volume fraction of pores in the as-built samples as a function of the carbon content. For comparison, the results for the raw powders (Fig. 7) are also plotted.
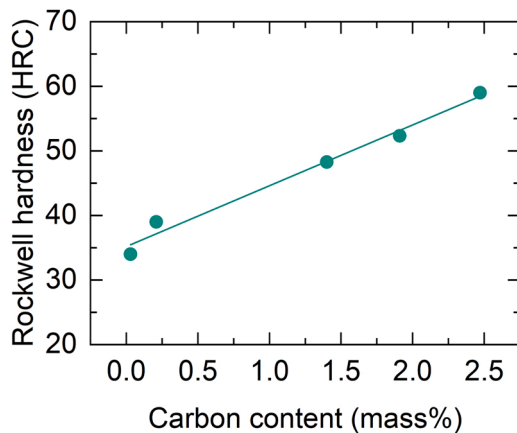

Fig. 15. Rockwell hardness of the as-built specimens as a function of the carbon content.

that the viscosity of molten Fe–C at the liquidus temperature monotonically increases with the increasing carbon content up to the eutectic composition. Thus, the use of the same building parameters for all the alloys would not cause a significant difference in the melt pool size between alloys, and each alloy would exhibit similar melt pool behavior.

One of the significant influences of carbon addition pertains to the significant reduction in the liquidus temperature (~130 K for investigated carbon concentrations), as depicted in Fig. 1. The wider temperature range (i.e., longer duration with the liquid phase) for the higher carbon alloys might allow more time for the pores in the melt pool to escape into the atmosphere. However, this scenario was not evidently observed in the studied alloys because the porosity of the 1.5C and 2.0C alloy samples did not facilitate pore removal during EB-PBF and represented the highest porosity at a carbon concentration of 2.0 mass% (Fig. 14).

The addition of carbon to the Co–Cr–Mo alloys decreases the liquidus temperature and alters the solidification behavior from the cellular growth to the dendritic mode and forms a eutectic microstructure in the 2.5C alloy (Fig. 10−12). The cellular solidification in the 0.04C and 0.22C alloys maintained a planar or smoother solidification front in directional solidification along the thermal gradient of the melt pool [74,75]. A eutectic structure comprising the γ-phase and carbide in the 2.5C alloy was formed owing to the migration of the locally smooth solid/liquid interface at the growth front. Allowing gas bubbles in the molten metal to accumulate in the liquid phase at the growth front and exit the solidified material to effectively remove the entrapped gas pores during the EB-PBF process. Fig. 1 shows the carbon in the alloys was partitioned into the liquid phase and the constitutional undercooling

ahead of the interface caused the breakdown of the planar front and resulted in dendritic growth, which was observed in alloys with carbon contents between 0.22 and 1.5 mass%. The dendritic growth is associated with the development of secondary dendrite arms growing in a direction perpendicular to the primary growth direction. This suggests that the complicated solid/liquid interfacial morphology would hinder the local melt flow, which consequently hinders the escape of the powder-originated gas bubbles from the melt pool. Therefore, the transition in the solidification behavior could be correlated with the powder-originated gas pores remaining in the EB-PBF process. These results showed that the solidification behavior strongly affected the porosity and its control in the PBF AM is vital for fabricating high-quality components with reduced porosity. Notably, our results also implicitly show that a similar strategy may be useful in other alloy systems.

5. Conclusions

The microstructure and porosity of the raw powder and the as-built specimens prepared by EB-PBF of Co–27Cr–6Mo (mass%) alloys with varying carbon concentrations (0.04–2.5 mass%) were investigated in this study. The correlation between the pore formation mechanisms and solidification behavior dependent on carbon concentration was discussed. The results obtained in this study can be summarized as follows:

- The prepared powders predominantly presented spherical shapes with similar particle size distributions showing a d_{50} value of approximately 50 μm. The high-carbon (1.5–2.5 mass%) powders contained larger particles ranging within 100–140 μm probably made of agglomerated granules (satellites), which were less present in the low-carbon powders.
- All raw powders contained spherical entrapped gas pores. The volume fraction of the porosity in the raw powders was ~0.10 vol.% for the 0.04C and 0.22C alloys to ~0.37 vol.% for the 2.5C alloy, thereby reflecting a direct increase with the carbon content. This could be correlated to the reduction in the liquidus temperature with an increased carbon content.
- Under identical building conditions, the 0.04C and 0.22C alloy specimens exhibited cellular solidification and dendritic microstructures with M_7C_3 carbide precipitation were observed in the 1.5C and 2.0C alloys. The as-built 2.5C alloy specimen exhibited a eutectic microstructure of the γ/ε matrix and M_7C_3 carbide precipitates.
- The entrapped gas pores in the 0.04C and 0.22C powders were almost completely eliminated during the EB-PBF process. The porosity of the raw powders of 1.5C and 2.0C alloys exhibited a minimal reduction after the EB-PBF process, which indicated a dependence on the carbon concentration. A further increase in the carbon concentration resulted in a significant reduction in the porosity.
- The observed dependence of the porosity on the carbon concentration after EB-PBF fabrication could be correlated to the solidification behavior. The smoother and flat solidification front in the cellular and eutectic solidification could effectively eliminate gas bubbles from the melt pool, whereas the complicated morphology at the solid/liquid interfaces of the dendritic growth possibly hindered pore elimination in the melt pool.
- Adding carbon significantly increased the Rockwell hardness of the as-built specimens, allowing them to reach a high value of HRC59 at 2.5C. Lack of a clear correlation between the hardness and porosity suggested that this improved hardness was primarily due to the formation of hard carbide precipitates, because the porosity in the as-built specimens was ~0.3 vol.% or lower.
- The present findings provide insights on the alloy design for reducing entrapped gas pores, which act as crack initiation sites, thereby contributing to the development of highly durable metal components via AM.

Funding source

CRediT authorship contribution statement

Shoya Aota: Investigation, Visualization, Formal analysis, Writing - original draft. **Kenta Yamanaka:** Conceptualization, Data curation, Investigation, Project administration, Resources, Supervision, Validation, Visualization, Writing - review & editing. **Manami Mori:** Investigation, Resources, Writing - review & editing. **Nobuyuki Sasaki:** Investigation. **Jérôme Adrien:** Investigation, Methodology, Resources, Supervision, Validation, Writing - review & editing. **Eric Maire:** Methodology, Resources, Supervision, Validation, Writing - review & editing. **Damien Fabrègue:** Conceptualization, Resources, Supervision, Validation, Writing - review & editing. **Akihiko Chiba:** Conceptualization, Funding acquisition, Resources, Supervision, Writing - review & editing.

Declaration of Competing Interest

The authors declare the following financial interests/personal relationships which may be considered as potential competing interests: One of the authors of this article is part of the Editorial Board of the journal. To avoid potential conflicts of interest, the responsibility for the editorial and peer-review process of this article lies with the journal's other editors. Furthermore, the concerned author was removed from the peer review process and had no, and will not have any access to confidential information related to the editorial process of this article.

Data Availability

Data will be made available on request.

Acknowledgement

Appendix A. Supporting information

Supplementary data associated with this article can be found in the online version at doi:10.1016/j.addma.2022.103134.

References

[1] A. Chiba, K. Kumagai, N. Nomura, S. Miyakawa, Pin-on-disk wear behavior in a like-on-like configuration in a biological environment of high carbon cast and low carbon forged Co–29Cr–6Mo alloys, Acta Mater. 55 (2007) 1309–1318, https://doi.org/10.1016/j.actamat.2006.10.005.

[2] S. Mischler, A.I. Muñoz, Wear of CoCrMo alloys used in metal-on-metal hip joints: a tribocorrosion appraisal, Wear 297 (2013) 1081–1094, https://doi.org/10.1016/j.wear.2012.11.061.

[3] Y. Chen, Y. Li, S. Kurosu, K. Yamanaka, N. Tang, Y. Koizumi, A. Chiba, Effects of sigma phase and carbide on the wear behavior of CoCrMo alloys in Hanks' solution, Wear 310 (2013) 51–62, https://doi.org/10.1016/j.wear.2013.12.010.

[4] Y. Koizumi, S. Suzuki, K. Yamanaka, B.-S. Lee, K. Sato, Y. Li, S. Kurosu, H. Matsumoto, A. Chiba, Strain-induced martensitic transformation near twin boundaries in a biomedical Co−Cr−Mo alloy with negative stacking fault energy, Acta Mater. 61 (2013) 1648–1661, https://doi.org/10.1016/j.actamat.2012.11.041.

[5] H.S. Dobbs, J.L.M. Robertson, Heat treatment of cast Co-Cr-Mo for orthopaedic implant use, J. Mater. Sci. 18 (1983) 391–401, https://doi.org/10.1007/BF00560627.

[6] A.J. Saldívar-García, H.F. López, Microstructural effects on the wear resistance of wrought and as-cast Co-Cr-Mo-C implant alloys, J. Biomed. Mater. Res. A 74A (2005) 269–274, https://doi.org/10.1002/jbm.a.30392.

[7] O. Öztürk, U. Türkan, A.E. Eroğlu, Metal ion release from nitrogen ion implanted CoCrMo orthopedic implant material, Surf. Coat. Technol. 200 (2006) 5687–5697, https://doi.org/10.1016/j.surfcoat.2005.08.113.

[8] K. Yamanaka, M. Mori, A. Chiba, Enhanced mechanical properties of as-forged Co–Cr–Mo–N alloys with ultrafine-grained structures, Metall. Mater. Trans. A 43 (2012) 5243–5257, https://doi.org/10.1007/s11661-012-1288-0.

[9] M. Mori, K. Yamanaka, S. Sato, S. Tsubaki, K. Satoh, M. Kumagai, M. Imafuku, T. Shobu, A. Chiba, Strengthening of biomedical Ni-free Co–Cr–Mo alloy by multipass "low-strain-per-pass" thermomechanical processing, Acta Biomater. 28 (2015) 215–224, https://doi.org/10.1016/j.actbio.2015.09.016.

[10] F. Ren, W. Zhu, K. Chu, Fabrication, tribological and corrosion behaviors of ultra-fine grained Co–28Cr–6Mo alloy for biomedical applications, J. Mech. Behav. Biomed. Mater. 60 (2016) 139–147, https://doi.org/10.1016/j.jmbbm.2015.12.039.

[11] K. Yamanaka, M. Mori, S. Sato, A. Chiba, Stacking-fault strengthening of biomedical Co–Cr–Mo alloy via multipass thermomechanical processing, Sci. Rep. 7 (2017) 10808, https://doi.org/10.1038/s41598-017-10305-1.

[12] E. Zhang, Y. Ge, G. Qin, Hot deformation behavior of an antibacterial Co–29Cr–6Mo–1.8Cu alloy and its effect on mechanical property and corrosion resistance, J. Mater. Sci. Technol. 34 (2018) 523–533, https://doi.org/10.1016/j.jmst.2016.09.025.

[13] K. Yamanaka, M. Mori, I. Kartika, M.S. Anwar, K. Kuramoto, S. Sato, A. Chiba, Effect of multipass thermomechanical processing on the corrosion behaviour of biomedical Co–Cr–Mo alloys, Corros. Sci. 148 (2019) 178–187, https://doi.org/10.1016/j.corsci.2018.12.009.

[14] N. Gong, I. Montes, K.C. Nune, R.D.K. Misra, K. Yamanaka, M. Mori, A. Chiba, Favorable modulation of osteoblast cellular activity on Zr-modified Co–Cr–Mo alloy: the significant impact of zirconium on cell–substrate interactions, J. Biomed. Mater. Res. B Appl. Biomater. 108 (2020) 1518–1526, https://doi.org/10.1002/jbm.b.34499.

[15] T. DebRoy, H.L. Wei, J.S. Zuback, T. Mukherjee, J.W. Elmer, J.O. Milewski, A. M. Beese, A. Wilson-Heid, A. De, W. Zhang, Additive manufacturing of metallic components – process, structure and properties, Prog. Mater. Sci. 92 (2018) 112–224, https://doi.org/10.1016/j.pmatsci.2017.10.001.

[16] D. Herzog, V. Seyda, E. Wycisk, C. Emmelmann, Additive manufacturing of metals, Acta Mater. 117 (2016) 371–392, https://doi.org/10.1016/j.actamat.2016.07.019.

[17] W.J. Sames, F.A. List, S. Pannala, R.R. Dehoff, S.S. Babu, The metallurgy and processing science of metal additive manufacturing, Int. Mater. Rev. 61 (2016) 315–360, https://doi.org/10.1080/09506608.2015.1116649.

[18] J.H. Martin, B.D. Yahata, J.M. Hundley, J.A. Mayer, T.A. Schaedler, T.M. Pollock, 3D printing of high-strength aluminium alloys, Nature 549 (2017) 365–369, https://doi.org/10.1038/nature23894.

[19] J.J. Lewandowski, M. Seifi, Metal additive manufacturing: A review of mechanical properties, Annu. Rev. Mater. Res. 46 (2016) 151–186, https://doi.org/10.1146/annurev-matsci-070115-032024.

[20] Y.M. Wang, T. Voisin, J.T. McKeown, J. Ye, N.P. Calta, Z. Li, Z. Zeng, Y. Zhang, W. Chen, T.T. Roehling, R.T. Ott, M.K. Santala, P.J. Depond, M.J. Matthews, A. V Hamza, T. Zhu, Additively manufactured hierarchical stainless steels with high strength and ductility, Nat. Mater. 17 (2018) 63–70, https://doi.org/10.1038/nmat5021.

[21] L.E. Murr, S.M. Gaytan, D.A. Ramirez, E. Martinez, J. Hernandez, K.N. Amato, P. W. Shindo, F.R. Medina, R.B. Wicker, Metal fabrication by additive manufacturing using laser and electron beam melting technologies, J. Mater. Sci. Technol. 28 (2012) 1–14, https://doi.org/10.1016/S1005-0302(12)60016-4.

[22] L.E. Murr, Metallurgy of additive manufacturing: Examples from electron beam melting, Addit. Manuf. 5 (2015) 40–53, https://doi.org/10.1016/j.addma.2014.12.002.

[23] R.R. Dehoff, M. Kirka, W.J. Sames, H. Bilheux, A.S. Tremsin, L.E. Lowe, S.S. Babu, Site specific control of crystallographic grain orientation through electron beam additive manufacturing, Mater. Sci. Technol. 31 (2015) 931–938, https://doi.org/10.1179/1743284714Y.0000000734.

[24] C. Körner, Additive manufacturing of metallic components by selective electron beam melting — a review, Int. Mater. Rev. 61 (2016) 361–377, https://doi.org/10.1080/09506608.2016.1176289.

[25] E.A.I. Ellis, M.A. Sprayberry, C. Ledford, J.P. Hankwitz, M.M. Kirka, C.D. Rock, T. J. Horn, Y. Katoh, R.R. Dehoff, Processing of tungsten through electron beam melting, J. Nucl. Mater. 555 (2021), 153041, https://doi.org/10.1016/j.nucmat.2021.153041.

[26] C. Rock, E. Lara-Curzio, B. Ellis, C. Ledford, D.N. Leonard, R. Kannan, M. Kirka, T. Horn, Additive Manufacturing of Pure Mo and Mo + TiC MMC Alloy by Electron Beam Powder Bed Fusion, JOM 72 (2020) 4202–4213, https://doi.org/10.1007/s11837-020-04442-8.

[27] S.H. Sun, Y. Koizumi, S. Kurosu, Y.P. Li, H. Matsumoto, A. Chiba, Build direction dependence of microstructure and high-temperature tensile property of Co–Cr–Mo alloy fabricated by electron beam melting, Acta Mater. 64 (2014) 154–168, https://doi.org/10.1016/J.ACTAMAT.2013.10.017.

[28] X.P. Tan, P. Wang, Y. Kok, W.Q. Toh, Z. Sun, S.M.L. Nai, M. Descoins, D. Mangelinck, E. Liu, S.B. Tor, Carbide precipitation characteristics in additive

manufacturing of Co-Cr-Mo alloy via selective electron beam melting, Scr. Mater. 143 (2018) 117–121, https://doi.org/10.1016/j.scriptamat.2017.09.022.

[29] Y. Zhao, Y. Koizumi, K. Aoyagi, D. Wei, K. Yamanaka, A. Chiba, Molten pool behavior and effect of fluid flow on solidification conditions in selective electron beam melting (SEBM) of a biomedical Co-Cr-Mo alloy, Addit. Manuf. 26 (2019) 202–214, https://doi.org/10.1016/j.addma.2018.12.002.

[30] Y. Zhao, Y. Koizumi, K. Aoyagi, D. Wei, K. Yamanaka, A. Chiba, Comprehensive study on mechanisms for grain morphology evolution and texture development in powder bed fusion with electron beam of Co–Cr–Mo alloy, Materialia 6 (2019), 100346, https://doi.org/10.1016/j.mtla.2019.100346.

[31] D.D. Xiang, P. Wang, X.P. Tan, S. Chandra, C. Wang, M.L.S. Nai, S.B. Tor, W.Q. Liu, E. Liu, Anisotropic microstructure and mechanical properties of additively manufactured Co–Cr–Mo alloy using selective electron beam melting for orthopedic implants, Mater. Sci. Eng. A 765 (2019), 138270, https://doi.org/10.1016/j.msea.2019.138270.

[32] A. Takaichi, Suyalatu, T. Nakamoto, N. Joko, N. Nomura, Y. Tsutsumi, S. Migita, H. Doi, S. Kurosu, A. Chiba, N. Wakabayashi, Y. Igarashi, T. Hanawa, Microstructures and mechanical properties of Co–29Cr–6Mo alloy fabricated by selective laser melting process for dental applications, J. Mech. Behav. Biomed. Mater. 21 (2013) 67–76, https://doi.org/10.1016/j.jmbbm.2013.01.021.

[33] G. Barucca, E. Santecchia, G. Majni, E. Girardin, E. Bassoli, L. Denti, A. Gatto, L. Iuliano, T. Moskalewicz, P. Mengucci, Structural characterization of biomedical Co–Cr–Mo components produced by direct metal laser sintering, Mater. Sci. Eng. C. 48 (2015) 263–269, https://doi.org/10.1016/j.msec.2014.12.009.

[34] B. Qian, K. Saeidi, L. Kvetková, F. Lofaj, C. Xiao, Z. Shen, Defects-tolerant Co-Cr-Mo dental alloys prepared by selective laser melting, Dent. Mater. 31 (2015) 1435–1444, https://doi.org/10.1016/j.dental.2015.09.003.

[35] X. Zhou, D. Wang, X. Liu, D.D. Zhang, S. Qu, J. Ma, G. London, Z. Shen, W. Liu, 3D-imaging of selective laser melting defects in a Co–Cr–Mo alloy by synchrotron radiation micro-CT, Acta Mater. 98 (2015) 1–16, https://doi.org/10.1016/j.actamat.2015.07.014.

[36] E. Liverani, A. Fortunato, A. Leardini, C. Belvedere, S. Siegler, L. Ceschini, A. Ascari, Fabrication of Co–Cr–Mo endoprosthetic ankle devices by means of Selective Laser Melting (SLM), Mater. Des. 106 (2016) 60–68, https://doi.org/10.1016/j.matdes.2016.05.083.

[37] S.L. Sing, S. Huang, W.Y. Yeong, Effect of solution heat treatment on microstructure and mechanical properties of laser powder bed fusion produced cobalt-28chromium-6molybdenum, Mater. Sci. Eng. A 769 (2020) 138511, https://doi.org/10.1016/j.msea.2019.138511.

[38] Z. Wang, S.Y. Tang, S. Scudino, Y.P. Ivanov, R.T. Qu, D. Wang, C. Yang, W. W. Zhang, A.L. Greer, J. Eckert, K.G. Prashanth, Additive manufacturing of a martensitic Co–Cr–Mo alloy: towards circumventing the strength–ductility trade-off, Addit. Manuf. 37 (2021), 101725, https://doi.org/10.1016/j.addma.2020.101725.

[39] Y. Zhao, K. Aoyagi, Y. Daino, K. Yamanaka, A. Chiba, Significance of powder feedstock characteristics in defect suppression of additively manufactured Inconel 718, Addit. Manuf. 34 (2020), 101277, https://doi.org/10.1016/j.addma.2020.101277.

[40] C. Pleass, S. Jothi, Influence of powder characteristics and additive manufacturing process parameters on the microstructure and mechanical behaviour of Inconel 625 fabricated by Selective Laser Melting, Addit. Manuf. 24 (2018) 419–431, https://doi.org/10.1016/j.addma.2018.09.023.

[41] S.E. Brika, M. Letenneur, C.A. Dion, V. Brailovski, Influence of particle morphology and size distribution on the powder flowability and laser powder bed fusion manufacturability of Ti-6Al-4V alloy, Addit. Manuf. 31 (2020), 100929, https://doi.org/10.1016/j.addma.2019.100929.

[42] S. Tammas-Williams, H. Zhao, F. Léonard, F. Derguti, I. Todd, P.B. Prangnell, XCT analysis of the influence of melt strategies on defect population in Ti-6Al-4V components manufactured by Selective Electron Beam Melting, Mater. Charact. 102 (2015) 47–61, https://doi.org/10.1016/j.matchar.2015.02.008.

[43] X. Shui, K. Yamanaka, M. Mori, Y. Nagata, K. Kurita, A. Chiba, Effects of post-processing on cyclic fatigue response of a titanium alloy additively manufactured by electron beam melting, Mater. Sci. Eng. A 680 (2017) 239–248, https://doi.org/10.1016/j.msea.2016.10.059.

[44] R. Cunningham, A. Nicolas, J. Madsen, E. Fodran, E. Anagnostou, M.D. Sangid, A. D. Rollett, Analyzing the effects of powder and post-processing on porosity and properties of electron beam melted Ti-6Al-4V, Mater. Res. Lett. 5 (2017) 516–525, https://doi.org/10.1080/21663831.2017.1340911.

[45] S. Tammas-Williams, P.J. Withers, I. Todd, P.B. Prangnell, Porosity regrowth during heat treatment of hot isostatically pressed additively manufactured titanium components, Scr. Mater. 122 (2016) 72–76, https://doi.org/10.1016/j.scriptamat.2016.05.002.

[46] T. Persenot, A. Burr, G. Martin, J.Y. Buffiere, R. Dendievel, E. Maire, Effect of build orientation on the fatigue properties of as-built Electron Beam Melted Ti-6Al-4V alloy, Int. J. Fatigue 118 (2019) 65–76, https://doi.org/10.1016/j.ijfatigue.2018.08.006.

[47] H. Toda, T. Inamori, K. Horikawa, K. Uesugi, A. Takeuchi, Y. Suzuki, M. Kobayashi, Effects of hydrogen micro pores on mechanical properties in A2024 aluminum alloys, Mater. Trans. 54 (2013) 2195–2201, https://doi.org/10.2320/matertrans.L-M2013832.

[48] E. Maire, P.J. Withers, Quantitative X-ray tomography, Int. Mater. Rev. 59 (2014) 1–43, https://doi.org/10.1179/1743280413Y.0000000023.

[49] C. Petit, E. Maire, S. Meille, J. Adrien, S. Kurosu, A. Chiba, CoCrMo cellular structures made by electron beam melting studied by local tomography and finite element modelling, Mater. Charact. 116 (2016) 48–54, https://doi.org/10.1016/j.matchar.2016.04.006.

[50] A. Chiba, Y. Daino, K. Aoyagi, K. Yamanaka, Smoke suppression in electron beam melting of Inconel 718 alloy powder based on insulator–metal transition of surface oxide film by mechanical stimulation, Materials 14 (2021) 4662, https://doi.org/10.3390/ma14164662.

[51] Z.C. Cordero, H.M. Meyer, P. Nandwana, R.R. Dehoff, Powder bed charging during electron-beam additive manufacturing, Acta Mater. 124 (2017) 437–445, https://doi.org/10.1016/j.actamat.2016.11.012.

[52] J.Y. Buffiere, E. Maire, J. Adrien, J.P. Masse, E. Boller, In situ experiments with X ray tomography: An attractive tool for experimental mechanics, Exp. Mech. 50 (2010) 289–305, https://doi.org/10.1007/s11340-010-9333-7.

[53] J. Ollion, J. Cochennec, F. Loll, C. Escudé, T. Boudier, TANGO: a generic tool for high-throughput 3D image analysis for studying nuclear organization, Bioinformatics 29 (2013) 1840–1841, https://doi.org/10.1093/bioinformatics/btt276.

[54] K. Heim, F. Bernier, R. Pelletier, L.P. Lefebvre, High resolution pore size analysis in metallic powders by X-ray tomography, Case Stud. Nondestruct. Test. Eval. 6 (2016) 45–52, https://doi.org/10.1016/j.csndt.2016.09.002.

[55] J. Schindelin, I. Arganda-Carreras, E. Frise, V. Kaynig, M. Longair, T. Pietzsch, S. Preibisch, C. Rueden, S. Saalfeld, B. Schmid, J.Y. Tinevez, D.J. White, V. Hartenstein, K. Eliceiri, P. Tomancak, A. Cardona, Fiji: An open-source platform for biological-image analysis, Nat. Methods 9 (2012) 676–682, https://doi.org/10.1038/nmeth.2019.

[56] G. Wegmann, R. Gerling, F.P. Schimansky, Temperature induced porosity in hot isostatically pressed gamma titanium aluminide alloy powders, Acta Mater. 51 (2003) 741–752, https://doi.org/10.1016/S1359-6454(02)00465-2.

[57] M.N. Ahsan, A.J. Pinkerton, R.J. Moat, J. Shackleton, A comparative study of laser direct metal deposition characteristics using gas and plasma-atomized Ti-6Al-4V powders, Mater. Sci. Eng. A 528 (2011) 7648–7657, https://doi.org/10.1016/j.msea.2011.06.074.

[58] R. Cunningham, S.P. Narra, C. Montgomery, J. Beuth, A.D. Rollett, Synchrotron-based X-ray microtomography characterization of the effect of processing variables on porosity formation in laser power-bed additive manufacturing of Ti-6Al-4V, JOM 69 (2017) 479–484, https://doi.org/10.1007/s11837-016-2234-1.

[59] W. Tillmann, C. Schaak, J. Nellesen, M. Schaper, M.E. Aydinöz, K.P. Hoyer, Hot isostatic pressing of IN718 components manufactured by selective laser melting, Addit. Manuf. 13 (2017) 93–102, https://doi.org/10.1016/j.addma.2016.11.006.

[60] B.H. Rabin, G.R. Smolik, G.E. Korth, Characterization of entrapped gases in rapidly solidified powders, Mater. Sci. Eng. A 124 (1990) 1–7, https://doi.org/10.1016/0921-5093(90)90328-Z.

[61] T. Fukuda, Y. Ohashi, K. Koshiro, Behavior of inert gas contamination in high ni alloy powder and consolidated powder material, Tetsu-to-Hagane 82 (1996) 623–627, https://doi.org/10.2355/tetsutohagane1955.82.7_623.

[62] X. Liang, E.J. Lavernia, Solidification and microstructure evolution during spray atomization and deposition of Ni$_3$Al, Mater. Sci. Eng. A 161 (1993) 221–235, https://doi.org/10.1016/0921-5093(93)90517-I.

[63] K. Isonishi, M. Tokizane, Production of Ti-alloy powder by rotating electrode process, Tetsu-to Hagane 76 (2017) 2108–2115, https://doi.org/10.2355/tetsutohagane1955.76.12_2108.

[64] Y. Zhao, Y. Koizumi, K. Aoyagi, K. Yamanaka, A. Chiba, Isothermal γ → ε phase transformation behavior in a Co-Cr-Mo alloy depending on thermal history during electron beam powder-bed additive manufacturing, J. Mater. Sci. Technol. 50 (2020) 162–170, https://doi.org/10.1016/j.jmst.2019.11.040.

[65] T. Takashima, Y. Koizumi, Y. Li, K. Yamanaka, T. Saito, A. Chiba, Effect of building position on phase distribution in Co-Cr-Mo alloy additive manufactured by electron-beam melting, Mater. Trans. 57 (2016) 2041–2047, https://doi.org/10.2320/matertrans.Y-M2016826.

[66] K. Yamanaka, M. Mori, A. Chiba, Nanoarchitectured Co−Cr−Mo orthopedic implant alloys: Nitrogen-enhanced nanostructural evolution and its effect on phase stability, Acta Biomater. 9 (2013) 6259–6267, https://doi.org/10.1016/j.actbio.2012.12.013.

[67] K. Yamanaka, M. Mori, A. Chiba, Effects of nitrogen addition on microstructure and mechanical behavior of biomedical Co−Cr−Mo alloys, J. Mech. Behav. Biomed. Mater. 29 (2014) 417–426, https://doi.org/10.1016/j.jmbbm.2013.10.006.

[68] K. Yamanaka, M. Mori, K. Sato, A. Chiba, Characterisation of nanoscale carbide precipitation in as-cast Co−Cr−W-based dental alloys, J. Mater. Chem. B 4 (2016) 1778–1786, https://doi.org/10.1039/c6tb00040a.

[69] R.J. Hebert, Viewpoint: Metallurgical aspects of powder bed metal additive manufacturing, J. Mater. Sci. 51 (2016) 1165–1175, https://doi.org/10.1007/s10853-015-9479-x.

[70] X. Zhan, Y. Zhao, Z. Liu, Q. Gao, H. Bu, Microstructure and porosity characteristics of 5A06 aluminum alloy joints using laser-MIG hybrid welding, J. Manuf. Process. 35 (2018) 437–445, https://doi.org/10.1016/j.jmapro.2018.08.011.

[71] S.M.H. Hojjatzadeh, N.D. Parab, W. Yan, Q. Guo, L. Xiong, C. Zhao, M. Qu, L. I. Escano, X. Xiao, K. Fezzaa, W. Everhart, T. Sun, L. Chen, Pore elimination mechanisms during 3D printing of metals, Nat. Commun. 10 (2019) 3088, https://doi.org/10.1038/s41467-019-10973-9.

[72] M. Watanabe, Y. Watanabe, C. Koyama, T. Ishikawa, S. Imaizumi, M. Adachi, M. Ohtsuka, A. Chiba, Y. Koizumi, H. Fukuyama, Density, surface tension, and viscosity of Co-Cr-Mo melts measured using electrostatic levitation technique, Thermochim. Acta 710 (2022), 179183, https://doi.org/10.1016/j.tca.2022.179183.

[73] G. Feng, K. Jiao, J. Zhang, S. Gao, High-temperature viscosity of iron-carbon melts based on liquid structure:The effect of carbon content and temperature, J. Mol. Liq. 330 (2021), 115603, https://doi.org/10.1016/j.molliq.2021.115603.

[74] L.H. Ungar, R.A. Brown, Cellular interface morphologies in directional solidification. The one-sided model, Phys. Rev. B 29 (1984) 1367–1380, https://doi.org/10.1103/PhysRevB.29.1367.

[75] G. Heiberg, K. Nogita, A.K. Dahle, L. Arnberg, Columnar to equiaxed transition of eutectic in hypoeutectic aluminium–silicon alloys, Acta Mater. 50 (2002) 2537–2546, https://doi.org/10.1016/S1359-6454(02)00081-2.